RESEARCH ARTICLE

Mind the gap: a new insight into the tip leakage vortex using stereo-PIV

Matthieu Dreyer · Jean Decaix · Cécile Münch-Alligné · Mohamed Farhat

Abstract The tip leakage vortex (TLV), which develops in the clearance between the rotor and the stator of axial hydro turbines, has been studied for decades. Yet, many associated phenomena are still not understood. For instance, it remains unclear how the clearance size is related to the occurrence of cavitation in the vortex, which can lead to severe erosion. Experiments are here carried out on the influence of the clearance size on the tip vortex structure in a simplified case study. A NACA0009 hydrofoil is used as a generic blade in a water tunnel while the clearance between the blade tip and the wall is varied. The 3D velocity fields are measured using Stereo Particle Image Velocimetry (SPIV) in three planes located downstream of the hydrofoil for different values of the upstream velocity, the incidence angle and a large number of tip clearances. The influence of the flow conditions on the structure of the TLV is described through changes in the vortex intensity, core axial flow, vortex center position and wandering motion amplitude. Moreover, high-speed visualizations are used to highlight the vortex core trajectory and clearance flow alteration, turning into a wall jet as the tip clearance is reduced. The measurements clearly reveal the existence of a specific tip clearance for which the vortex strength is maximum and most prone to generating cavitation.

List of symbols

c	Hydrofoil chord
h	Maximum foil thickness
W_∞	Inlet velocity
p_∞	Inlet pressure
x, y, z	Cartesian coordinates
u, v, w	Spanwise, transverse and axial velocity
x_c, y_c	Vortex center coordinates
r_c	Vortex core radius
Re_c	Reynolds number ($W_\infty c/\nu$)
α	Incidence angle
τ	Normalized tip clearance (gap/h)
ω	Vorticity
Γ	Circulation
Γ^*	Normalized circulation ($\Gamma/W_\infty r_c$)
Γ_∞^*	Γ^* at $\tau = 2$
$C_{P_{min}}$	Pressure coefficient in the vortex center $\left(\dfrac{p(r=0) - p_\infty}{\frac{1}{2}\rho W_\infty^2} \right)$

M. Dreyer (✉) · M. Farhat
Laboratory for Hydraulic Machines, Ecole polytechnique fédérale de Lausanne, Av. de Cour 33 bis, 1007 Lausanne, Switzerland
e-mail: matthieu.dreyer@epfl.ch

J. Decaix · C. Münch-Alligné
Institut Systèmes industriels, HES-SO Valais-Wallis, Route du Rawyl 47, 1950 Sion, Switzerland

1 Introduction

Tip vortices are prevalent in many industrial applications (e.g., air transportation, marine propulsion, wind turbines, hydraulic machines, space rockets). The need to understand and control the dynamics of these flows has driven numerous researches, producing an abundant literature [see Green (1995) and Arndt (2002) for a review]. From a theoretical point of view, the model of Batchelor (1964), valid far downstream of the wing tip, is widely used to describe the structure of the trailing vortex flow. Moore and Saffman (1973)

developed a more sophisticated model, valid in the intermediate region between the completion of roll-up and the far field, where the Batchelor solution holds. Recently, Pino et al. (2011) used SPIV to measure the 3D velocity field in the tip vortex behind a foil. Better agreement with the model of Moore and Saffman than that of Batchelor was observed. In axial turbomachinery, a leakage flow occurs between the blade tip and the casing, driven by the pressure difference between the blade pressure and suction sides. The vorticity shed by this leakage flow rolls up into the so-called tip leakage vortex (TLV), which is strongly influenced by the vicinity of the wall (confinement). In axial hydraulic machines, cavitation may develop in the core of TLVs, leading sometimes to severe erosion of the runner blades and the casing, as well as an increase in structural vibrations. Farrell and Billet (1994) have found that cavitation incipience in an axial pump may be delayed if the tip clearance is set to an optimum value of about 0.2 times the maximum blade thickness. Boulon et al. (1999) examined the effect of the clearance size on the tip vortex generated by an elliptical foil in a setup without relative motion between the end wall and the foil. They found, conversely, that the cavitation inception index increases as the gap is reduced, while no tip vortex cavitation was observed in the most confined cases. Similar observations were reported by Gopalan et al. (2002) for the case of a cambered hydrofoil in a water tunnel. More recently, Wu et al. (2011) and Miorini et al. (2012) studied experimentally the internal structure of the TLV within the rotor of an axial waterjet pump using both 2D and stereo-PIV. They observed that the instantaneous TLV structure is composed of unsteady vortex filaments that propagate into the tip region of the blade passage and roll up into the TLV. They noticed that vortex breakdown could also occur as the TLV migrated toward the pressure side of the neighboring blade, changing drastically the vortex characteristics, as reported by Pasche et al. (2014). The measured velocity fields in these studies were, however, limited to a few tip clearance values.

In the specific area of Kaplan turbines, the wake of the distributor guide vanes produces a highly non-uniform pressure field, which leads to repetitive collapses and rebounds of the cavitating tip vortices. Obviously, cavitation erosion depends not only on the vortex strength and core size, but also on its trajectory and how far it stands from solid boundaries. It should be noted that, nowadays, it is still not possible to fairly predict cavitation occurrence in axial turbines, neither from numerical simulations nor from reduced scale model tests. In their attempt to mitigate the cavitation development in axial turbines, engineers commonly implement the so-called anti-cavitation lip, which consist of a simple winglet attached to the tip of the blades. Nevertheless, such a remedy often fails to reduce cavitation erosion, as reported by Roussopoulos and Monkewitz (2000) on a simplified case study.

In the present study, the structure and trajectory of a TLV generated at the tip of a fixed 2D hydrofoil are investigated experimentally for different confinements and flow parameters. Our objective is to perform accurate measurements of the velocity field to better understand the underlying physics of vortex confinement and provide an extensive experimental database for further developments. In our simplified approach, the effect of relative motion between the rotating blades and the casing of an axial turbine is not taken into account. It is assumed that the mean vortex flow is not fundamentally altered by the end wall motion, as already shown by Wang and Devenport (2004).

It is well known that velocity measurements in vortical structures are subjected to uncertainty due to the wandering phenomenon, which is a random displacement of the vortex centerline with amplitude of the order of the vortex core size. Although this phenomenon has been well referenced, its origin remains unclear. It is presumed to arise from a resonant excitation triggered by the free-stream turbulence (Fabre et al. 2008). As a consequence, single point measurement techniques, such as Laser Doppler Velocimetry (LDV), always result in a more diffuse velocity field than in reality, and correction methods must be applied to retrieve the true velocity field, cf. Devenport et al. (1996); Iungo et al. (2009); and Pasche et al. (2014). Furthermore, the finite size of the LDV measurement volume introduces another smoothing effect that must also be accounted for (Le Guen et al. 1997). Therefore, we have selected the SPIV technique for the measurement of the 3D velocity field, since it leaves the possibility of accurately filtering out this wandering through various processing tools, as those proposed, for instance, by Bhagwat and Ramasamy (2012).

2 Experimental setup

2.1 Case study and setup

The experiments are carried out in the EPFL high-speed cavitation tunnel. The squared test section is 150 mm wide and 750 mm long. A honeycomb and a contraction nozzle (ratio 46:1) upstream of the test section ensure a low turbulence level (below 1 %). The maximum inlet flow velocity is 50 m/s. The static pressure in the test section can be varied from near vacuum up to 10 bars. The operating flow parameters are the upstream velocity W_∞, the pressure in the test section inlet p_∞, and the hydrofoil incidence angle α. The test section walls are made of 80-mm-thick plexiglass, providing a good optical access to the flow. The TLV is generated by a stainless steel NACA0009 hydrofoil with a thickness distribution y_b given by Eq. (1), using $c_0 = 110$ mm for the chord length. The foil is truncated at $c = 100$ mm, its span is 150 mm, and its maximum thickness h is

9.9 mm. The foil tip pressure side corner was rounded with a small radius of 1 mm in order to limit the cavitation in the clearance during the flow visualizations. It is mounted on a sliding support allowing for an adjustable clearance (or gap) between the foil tip and the test section lateral wall. The gap can be varied smoothly between 0 and 20 mm. The influence of the foil boundary-layer state is also investigated by testing smooth and roughened leading edge. The turbulent boundary-layer can be tripped with a 4-mm-wide strip of distributed roughness, made of glue and 125-μm-diameter sand. The roughness is placed on both sides of the hydrofoil, 4 mm downstream of the leading edge, as described by Ausoni et al. (2012).

The results are represented in the Cartesian x, y, z coordinate system. Its origin is located on the test section lateral wall, corresponding to the plane $x = 0$, while the foil axis of rotation is on the intersection of the planes $y = 0$ and $z = 0$. The orientation of the coordinate system is illustrated in Fig. 1.

$$\frac{y_b}{c_0} = \begin{cases} a_0 \left(\frac{x}{c_0}\right)^{1/2} + a_1 \left(\frac{x}{c_0}\right) \\ + a_2 \left(\frac{x}{c_0}\right)^2 + a_3 \left(\frac{x}{c_0}\right)^3 \end{cases} \quad 0 \le \frac{x}{c_0} \le 0.5$$

$$\frac{y_b}{c_0} = \begin{cases} b_0 + b_1 \left(1 - \frac{x}{c_0}\right) \\ + b_2 \left(1 - \frac{x}{c_0}\right)^2 + b_3 \left(1 - \frac{x}{c_0}\right)^3 \end{cases} \quad 0.5 < \frac{x}{c_0} \le 1.0$$

$$\begin{aligned} a_0 &= +0.1737 & b_0 &= +0.0004 \\ a_1 &= -0.2422 & b_1 &= +0.1737 \\ a_2 &= +0.3046 & b_2 &= -0.1898 \\ a_3 &= -0.2657 & b_3 &= +0.0387 \end{aligned} \quad (1)$$

2.2 Flow investigations

SPIV is used to measure the 3D velocity field in three cross-sections of the tip vortex at different downstream locations (see Fig. 1). A 2-mm-wide laser sheet is generated by a double-pulsed YAG laser (Litron DualPower, 200 mJ/pulse, 532 nm wavelength) and a cylindrical lens. The time interval between laser pulses is set for each inlet velocity in order to limit the maximum out-of-plane displacement of the seeding particles to one-tenth of the laser sheet thickness (e.g., 30 μs for $W_\infty = 5$ m/s). Image pairs are acquired using two CCD cameras (Dantec FlowSense E0 4M) with a resolution of 2,048 × 2,048 pixels. The cameras are mounted on both sides of the laser sheet with an orientation of 30° with respect to the latter. To minimize the optical distortions, a transparent water box is mounted on the lateral wall. Its fixation is ensured by creating a partial vacuum, allowing for a simple positioning procedure. Two 60-mm lenses are used in combination with Scheimpflug mounts to align the focal plane with the laser sheet. The laser and the cameras are mounted on a joint support and moved to different downstream positions with a 2D traversing system.

Fluorescent particles (polyamide particles, 20 μm average diameter) are used as seeding material. Rhodamine B dye is encapsulated in the particles following an in-house cost-effective method, as described by Müller et al. (2013). The fluorescent dye emits orange light at a wavelength of around 620 nm when excited with the laser. The cameras are equipped with long-pass filters, discarding wavelengths shorter than 570 nm. Therefore, only the light scattered by
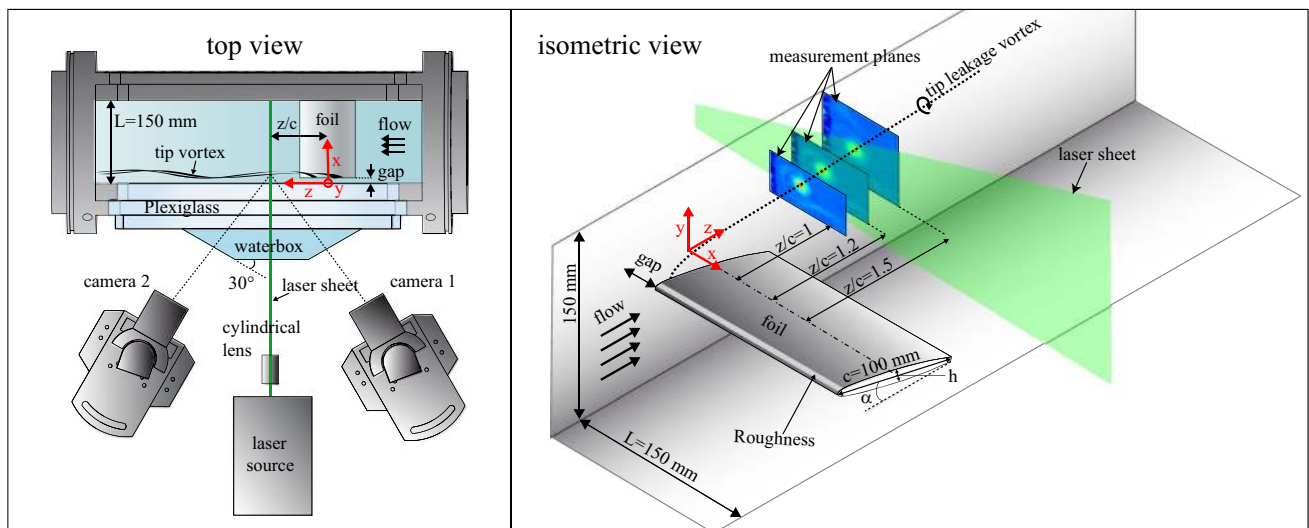
Fig. 1 Sketch of the SPIV configuration used in the 3D measurement of the velocity field. *Left* top view of the tunnel test section and optical instruments. *Right* isometric view of the inlet test section with the three measurement planes

the particles is recorded. The out-of-plane velocity component is obtained by combining the 2D velocity fields derived for each camera. A third-order polynomial calibration ensures the conversion between the camera reference frame and the real physical dimensions. To this end, a 100×100 mm double-faced doted target (dots separated by 2.5 mm) is immersed in the test section and is imaged at several positions within the width of the laser sheet. The accuracy of the calibration is verified by comparing the streamwise velocity profiles (corresponding to the out-of-plane component) measured by SPIV with that measured by LDV, see Fig. 2. Excellent agreement in the velocity data is observed. The large standard deviation in the wall boundary-layer measured by the LDV is due to the finite size of the control volume (about 1.2 mm) in a region of high velocity gradients.

Finally, cavitation in the TLV core is used as a tracer to follow the vortex trajectory. A high-speed camera (Photron SA1.1) along with a xenon flash light (11-ms duration and 1.1-KJ energy) is used to visualize the cavitating TLV dynamics at 20,000 frames per second for several flow regimes.

3 Analysis methodology

3.1 Flow parameters and PIV processing

The velocity field is measured in a cavitation-free regime at three streamwise positions ($z/c = 1, 1.2$ and 1.5) downstream of the hydrofoil. At each position, five incidence angles ($3°, 5°, 7°, 10°, 12°$) are tested in combination with up to four inlet velocities (5, 10, 15 and 20 m/s). The Reynolds number based on the foil chord $Re_c = W_\infty c/\nu$ varies from 5×10^5 to 2×10^6. For each of these configurations, the tip clearance is varied between 0 and 20 mm. Moreover, measurements are performed both with
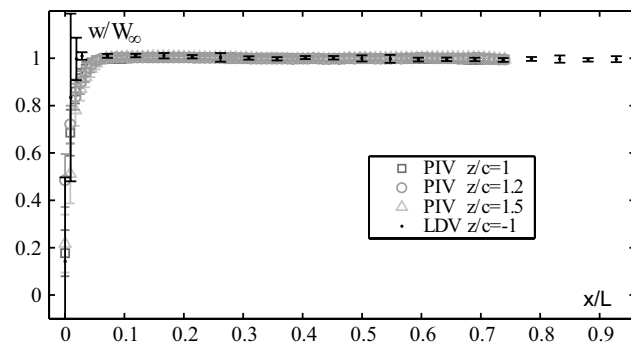
and without the turbulent boundary-layer tripping on the hydrofoil leading edge, yielding a total of 1,170 distinct configurations.

The velocity fields are derived by processing the acquired image pairs with an adaptive multi-pass correlation algorithm, which adjusts the size and shape of the individual Interrogation Areas (IAs) with the local seeding densities and flow gradients. The criterion for the IA size is the presence of at least eight particles and a minimum of 16×16 pixels. A total of 182×120 velocity vectors with a spatial resolution of 0.6 mm are finally obtained. The vector fields are validated with a universal outlier test, and spurious vectors are replaced by the median value of the 5×5 neighboring vectors. The percentage of spurious vectors is around 5 %. The measurement errors are estimated assuming a 0.1 pixel uncertainty on the measurement of particle displacements (Westerweel 2000). Since both cameras contribute symmetrically to the measurements, the in-plane errors are smaller by a factor $1/\sqrt{2}$ than the value for the single camera arrangement and the error of the out-of-plane component equals the in-plane error multiplied by $1/\tan(\phi)$ (Prasad 2000), where ϕ is the angle between the light sheet normal and the camera viewing direction. Given an average particle displacement of 5 pixels, the uncertainties were estimated to 1.4 % for the in-plane components and 0.8 % for the out-of plane component. This is in accordance with Fig. 2 which gives <1 % error for the out-of-plane component. The average velocity field is determined after processing 100 individual vector fields for each operating condition. It is verified that increasing this number does not affect the mean flow characteristics.

The streamwise vorticity $\omega = \partial v/\partial x - \partial u/\partial y$ is computed by the numerical differentiation of the velocity field. To minimize bias errors and avoid any undesirable effect of the differentiation of a noisy field, the spatial sampling resolution is increased via a least-square cubic spline interpolation of the velocity. The derivatives are then estimated with the following fourth-order Richardson numerical scheme:

$$\omega_{i,j} = \frac{1}{12\Delta X}(-v_{i+2,j} + 8v_{i+1,j} - 8v_{i-1,j} + v_{i-2,j})$$
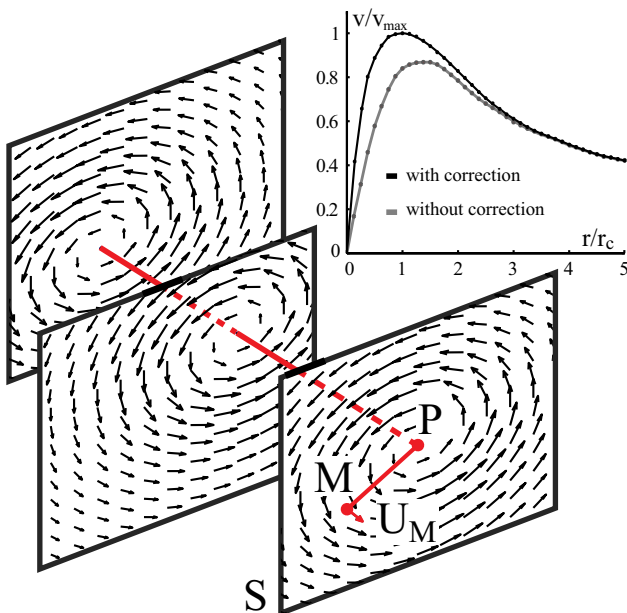$$- \frac{1}{12\Delta Y}(-u_{i,j+2} + 8u_{i,j+1} - 8u_{i,j-1} + u_{i,j-2}) \quad (2)$$

3.2 Wandering correction

Wandering is a random fluctuation of the vortex axis with an amplitude comparable to the vortex core size. If not corrected, the wandering would yield to a larger core size and a lower value of the maximum velocity in the mean vortex flow, as mentioned previously.

Fig. 2 Comparison of the axial velocity profiles in the test section measured by PIV and LDV. No hydrofoil is mounted in the test section

Several techniques are available to retrieve the swirl center such as the local partial orthogonal decomposition used by Bouillot et al. (2014). In our case, we have implemented the algorithm of Graftieaux et al. (2001) to identify the vortex center and align the velocity maps before averaging, as illustrated in Fig. 3. Introducing the dimensionless scalar function Π at the position P, defined as:

$$\Pi(P) = \frac{1}{N} \sum_S \frac{(PM \wedge U_M) \cdot z}{\|PM\| \cdot \|U_M\|} \tag{3}$$

where S is a rectangular domain of fixed size centered on P, M lies in S, z is the unit vector normal to the measurement plane, U_M is the velocity vector and N is the number of velocity vectors inside S, as specified in Fig. 3. The function Π reaches a maximum equal to one at the location of the vortex center if the vortex is axisymmetric, but it would be lower for an asymmetrical vortex. Graftieaux's algorithm is a simple yet highly robust way to identify the swirl center location of a velocity field. Unlike gradient-based vortex detection techniques, which are susceptible to experimental noise, Π does not require any gradient evaluation and considers only the topology of the velocity field. In general, the vortex center does not lie on a measurement grid node, and the realignment requires an interpolation of the measurement data. This is realized via the cubic spline interpolation of the velocity field mentioned previously.

3.3 Identification of the key vortex parameters

Tip vortices are characterized by two zones: the core, close to the center of rotation where the viscous effects are dominant, and an outer region where the motion is mainly irrotational. This behavior can be modeled using simple vortex models such as that of Rankine and Lamb-Oseen. Vatistas et al. (1991) proposed a simplified expression that encompasses a series of tangential velocity profiles for a vortex structure, which can be written in the form:

$$v_\theta(r) = \frac{\Gamma}{2\pi} \left(\frac{r}{(r_c^{2n} + r^{2n})^{1/n}} \right) \tag{4}$$
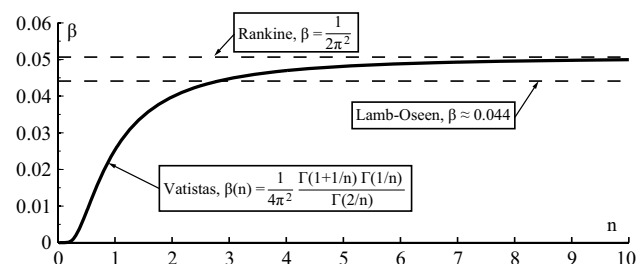
The Vatistas model is used here, since by varying the shape parameter n in Eq. (4), a wide range of velocity profiles can be defined. When $n = 1$, the Scully vortex is reproduced, the case $n \approx 2$ gives a close approximation to the Lamb-Oseen model, while $n \to \infty$ corresponds to the Rankine vortex (Bhagwat and Leishman 2002). The minimum pressure coefficient in the vortex center can be derived by integrating the equilibrium equation $\partial p/\partial r = \rho v_\theta^2/r$, leading to the following expression of the minimum pressure coefficient in the vortex center:

$$C_{p_{min}} = -\beta \left(\frac{\Gamma}{W_\infty r_c} \right)^2 \tag{5}$$

where β is a constant whose value depends on the choice of vortex model. For the Vatistas model, β is a function of the shape parameter n, as illustrated in Fig. 4, defined by:

$$\beta(n) = \frac{1}{4\pi^2} \frac{\Gamma(1 + 1/n)\Gamma(1/n)}{\Gamma(2/n)} \tag{6}$$

Notice that $\Gamma(n)$ denotes the Euler integral of the second kind (Gamma function), not to be confused with the circulation Γ. Equation (5) shows that the prediction of the minimum pressure in the vortex center effectively reduces to the estimation of two key parameters, namely the vortex circulation, Γ, and the viscous core radius, r_c. The circulation is calculated by integrating the vorticity within the

Fig. 3 *Left* correction of the wandering by aligning all the vortex centers before averaging. *Top right* example of the wandering effect on the circumferential velocity

Fig. 4 Value of β in Eq. (5). The curve $\beta(n)$ for the Vatistas model is plotted along with the Rankine and Lamb-Oseen β value

vortex core, the radius of which r_c is estimated by a best fit—in least-squares sense—of the Vatistas model with $n = 2$ over the measured velocity profiles.

4 Results and discussion

4.1 Flow visualizations

Cavitation can be a convenient way to visualize the trajectory of vortices, as reported by Chang et al. (2007). A reduction in the static pressure in the test section leads to the vaporization of the vortex core, which makes it visible. However, this is not a strictly passive means of flow visualization, as vapor can completely fill the vortex core, leading to vorticity redistribution and possible alterations of the flow dynamics. Figure 5 presents high-speed visualization snapshots of the cavitating TLV for different values of tip clearance. The inlet velocity is 10 m/s, the incidence angle is 10°, and p_∞ is kept to 1 bar for all clearances. To assess the mean TLV trajectory, we have summed the images captured during 11 ms at 20,000 FPS. The result is given in Fig. 6 for three tip clearances. The scatter of the cavitation bubbles in the vortex core unveils the wandering amplitude which is quite small in theses cases. Moreover, comparisons

with the TLV position in cavitation-free regime, obtained by SPIV and represented by the yellow crosses in Figs. 5 and 6, indicate that neither the vortex trajectory nor the wandering amplitude are altered by the cavitation.

The trajectory of the TLV strongly depends on the clearance size: the smaller the gap, the more the vortex is pulled away from the hydrofoil. This is due to a purely potential flow effect and can be understood through the consideration of a simple model consisting of a 2D vortex above a wall, as explained by Doligalski et al. (1994). To ensure zero flow across the wall, an image vortex is placed symmetrically to the actual TLV with respect to the confinement wall. This image vortex induces an upward velocity in the actual vortex, tending to move it upwards.

Another feature is the change in slope of the vortex trajectory at the foil trailing edge. This is particularly visible if the TLV remains relatively close to the foil along the chord, i.e., at large clearances values like $\tau = 2$. This phenomenon can again be explained with reference to the image system of the tip clearance flow. Over the foil, one must consider three images of the TLV to satisfy the relevant kinematic constraints, as reported by Chen et al. (1991). Two of the image vortices induce vertical velocities on the actual vortex that partially cancel out. After the blade, there is only one image vortex needed to satisfy the
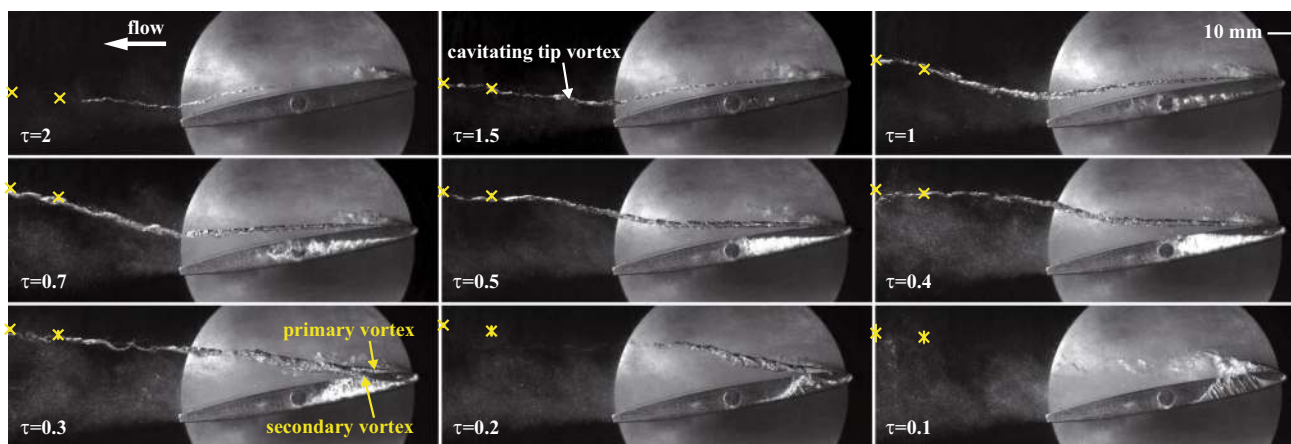
Fig. 5 Snapshots of the cavitating TLV generated by a NACA0009 for different gap widths. The tip clearance is viewed from the side and is facing the observer. The *yellow crosses* represent the position measured by SPIV in cavitation-free regime, in the planes $z/c = 1$ and 1.2. Flow conditions: $W_\infty = 10$ m/s, incidence = 10°, $p_\infty = 1$ bar. The original movies are provided as supplementary material


Fig. 6 Superposition of the cavitating TLV visualizations during 11 ms for three gap widths. The *yellow crosses* represent the position measured by SPIV in cavitation-free regime, in the planes $z/c = 1$ and 1.2. Flow conditions: $W_\infty = 10$ m/s, incidence = 10°, $p_\infty = 1$ bar

boundary conditions, and the resulting induced upward velocity is thus larger.

The amount of cavitation in the vortex core reveals the changes of the vortex strength along the chord. As the clearance is reduced, the cavitation becomes more intense, but the vortex also become less coherent. For the most confined configuration, the vortex rapidly loses its coherence until practically vanishing. Cavitation in the clearance region also appears when the gap is reduced. This results from boundary-layer separation in the gap and can be reduced when the edge of the foil pressure side is rounded, as explained by Laborde et al. (1997). Clearance cavitation indicates that the gap flow turns into a vertical wall jet as the gap is reduced, entraining vorticity filaments into the TLV. It also reveals that the TLV results from the merging of a primary vortex, originating at the leading edge, and a secondary vortex that develops in the clearance (visible in the cases $\tau = 0.3$ and 0.2, see also the movies provided as supplementary material). In fact, flow visualizations at low inlet pressure showed that the secondary vortex exists for all clearances. However, as it is weaker than the primary vortex, the secondary vortex is not visible on Fig. 5 for large clearances. The secondary and primary vortices systematically merge together, and the merging location moves toward the foil leading edge as the clearance is reduced.

4.2 TLV characteristics

The TLV is formed by the rolling up of the vorticity transported by the leakage flow which is driven by the pressure gradient across the clearance. Its characteristics depend on the operating conditions, such as the foil incidence angle, the inlet velocity and the wall proximity. Figure 7 illustrates the influence of the hydrofoil incidence on the TLV for a fixed normalized clearance $\tau = 1.5$. Vorticity maps with 2D streamlines are represented for two incidences, 5° and 12°, while the evolution of the vortex circulation Γ with the incidence is plotted below for the smooth and rough foil. The vorticity is concentrated in a small volume corresponding to the vortex viscous core while the rest of the flow is nearly irrotational. Small structures with negative vorticity are nonetheless produced in the boundary-layer on the test section wall. The streamlines indicate that the vortices are not perfectly axisymmetric. The reason for this is twofold: The test section wall alters the vortex symmetry by channeling the flow in the clearance, and the measurement plane is not perfectly orthogonal to the vortex axis, as visible in Fig. 5. The inclination angles between the measurement plane and the vortex can be identified following a procedure similar to that of Wall and Richard (2006). The velocity fields can then be projected into the vortex coordinate system. In fact, it was observed that the vortex properties (circulation and viscous core radius) vary <1 % due to the
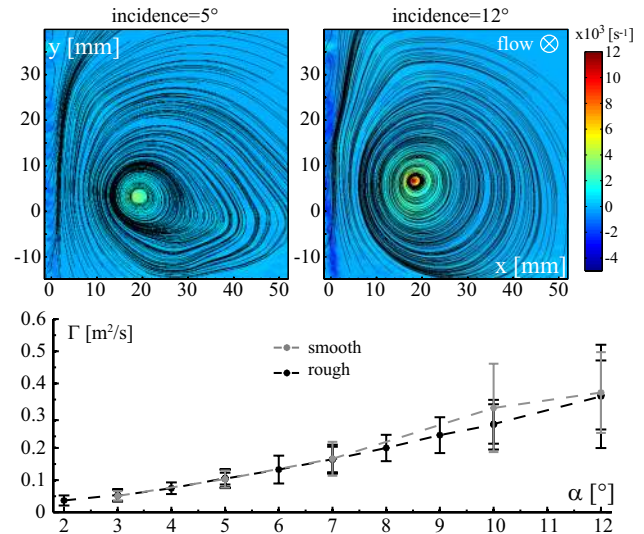
Fig. 7 Evolution of the TLV with incidence, $W_\infty = 10$ m/s, $\tau = 1.5$, $z/c = 1$. *Top* streamlines and norm of the streamwise vorticity, rough hydrofoil. *Bottom* vortex circulation relative to the incidence angle for the rough and smooth hydrofoil

Table 1 Vortex core size for $W_\infty = 10$ m/s, incidence = 7°, $\tau = 1.5$, $z/c = 1$

| Hydrofoil	Core size (mm)	Circulation (m²/s)
Smooth	3.8	0.166
Rough	4.2	0.165

vortex axis inclination. Consequently, and since the identification of the inclination angles is subject to uncertainty, the analysis of the TLV is performed in the measurement plane reference frame.

The vortex circulation Γ is directly proportional to the foil bound circulation Γ_0, which is linked to the lift coefficient C_L according to the Kutta–Joukowski theorem: $\Gamma_0 = 0.5cW_\infty C_L$. It thus comes as no surprise that the vortex circulation increases monotonically with the hydrofoil incidence angle. The vortex circulation follows the linear dependence of the lift coefficient with the incidence angle until the stall condition is reached (near 14° for the NACA0009). Rough and smooth hydrofoils generate nearly equal vortex circulations. The viscous core radius is, however, larger with the rough foil, see Table 1. Indeed, McCormick (1962) observed that the viscous core radius is related to the thickness of the boundary-layer on the pressure side surface near the foil tip, which is larger when the turbulent boundary-layer is tripped. Finally, it can be observed that the standard deviation of the measured circulation increases with the vortex intensity.

The influence of the *Re* number was investigated by varying the inlet velocity, see Fig. 8. The vortex circulation
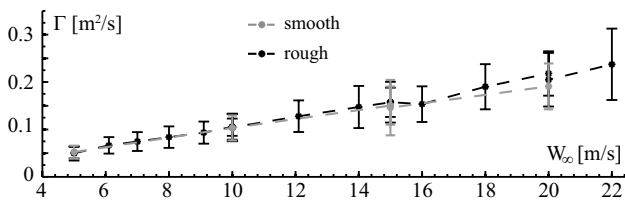
Fig. 8 Evolution of the vortex circulation with the inlet velocity for the rough and smooth hydrofoils, incidence = 5°, $\tau = 1.5$, $z/c = 1$
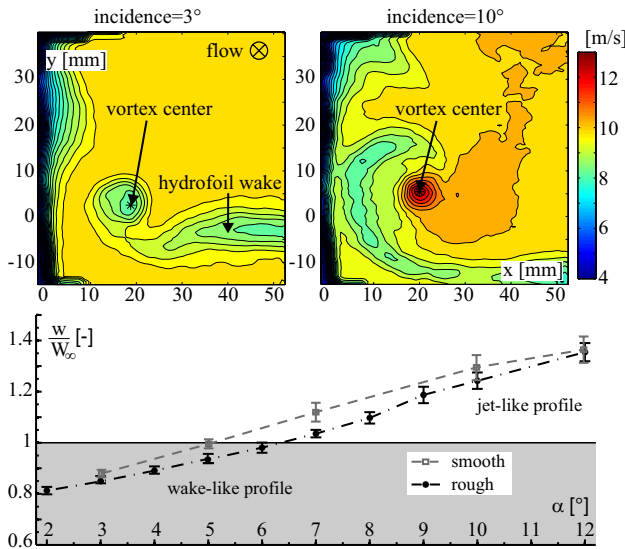
Fig. 9 Evolution of the axial velocity field, $W_\infty = 10$ m/s, $\tau = 1.5$, $z/c = 1$. *Top* isocontour of the axial flow, rough hydrofoil. *Bottom* axial velocity in the vortex center relative to the incidence angle for both the rough and smooth hydrofoils

follows the linear trend with the inlet velocity, as predicted by the Kutta–Joukowski theorem. Once again, smooth and rough hydrofoils generate similar vortex circulation while the standard deviation increases with the vortex strength. Increasing the inlet velocity does not greatly influence the TLV structure or position, though it yields a higher vortex intensity and a slightly smaller core size.

The evolution of the vortex core axial flow with the foil incidence angle is represented in Fig. 9. As the incidence increases, the axial flow in the vortex core features an interesting switchover angle for which it changes from wake-like to jet-like (Fig. 9, bottom). The isocontours of the axial flow (Fig. 9, top) reveal that a region with a deficit of velocity surrounds the TLV at 3° incidence. The wall boundary-layer can be seen on the left-hand side of the figure, while the wake of the hydrofoil is visible as a horizontal region with a velocity deficit. The TLV tends to roll up the fluid layers in its vicinity, entraining the hydrofoil wake and resulting in a complex axial velocity field. For the 10°

incidence, the vortex core axial flow is in contrast faster than the surrounding flow, even if the rolling up of the foil wake around the TLV is still visible.

The nature of the axial flow results from the balance between an inviscid effect, which tends to accelerate the flow, and the momentum defect originating in the foil boundary-layer that rolls up into the vortex core, resulting in a velocity deficit (Green 1995; Spalart 1998). From the application of Bernoulli's principle, Batchelor (1964) derived the following expression for the axial velocity in an idealized axisymmetric vortex:

$$w(r)^2 = W_\infty^2 + \int_r^\infty \frac{1}{4\pi^2 r'^2} \frac{\partial \Gamma^2}{\partial r'} \, \mathrm{d}r' - 2\Delta H \qquad (7)$$

where ΔH represents the viscous losses along a streamline passing through the boundary-layer of the hydrofoil. If the vorticity in the vortex is one-signed, as is normally the case, the second term on the right-hand side of Eq. (7) is strictly positive. An axial velocity excess in the vortex center—or a jet-like profile—is thus predicted in the absence of viscosity. The dissipation term ΔH competes with the inviscid acceleration mechanism to determine the nature of the resulting core axial flow. With the assumption of constant dissipation and vortex core radius, Eq. (7) states that an increase in the overall circulation results in a higher axial velocity in the vortex core. This is coherent with the fact that the switchover angle occurs earlier for the smooth foil—around 5° compared to 6° for the rough foil—since it generates a vortex with a smaller viscous core (cf. Table 1).

Lee and Pereira (2010) have observed that a jet-like axial flow is always present during the vortex formation but that interactions with the foil wake and shear layer are likely to change a jet-like axial flow to a wake-like axial flow for small incidence angles. For large incidence angles, they noticed that the vortex is surrounded by a shear layer, protecting it from outside disturbances. This roll up of the shear layer around the TLV is also observed in the present experiment, although measurements in the vortex formation region—i.e., over the hydrofoil—would be necessary to confirm their observations.

For a better representation of the velocity field, Fig. 10 illustrates the 3D streamlines with some tracing particles for two different incidence angles (5° and 10°, flow conditions: $W_\infty = 10$ m/s, $\tau = 1.5$). Twenty-five streamlines are initiated in the measurement plane $z/c = 1$ on a vertical line. Since the TLV properties vary little with the downstream distance, the velocity field is interpolated linearly between the three measurement planes. The pitch in the helix formed by the streamlines illustrates the vortex swirl number, i.e., the ratio between the circumferential and axial velocities. Higher incidence angles produce higher swirl in the flow. The tracing particles highlight the vortex core axial flow. For a 5° incidence angle, the core axial velocity
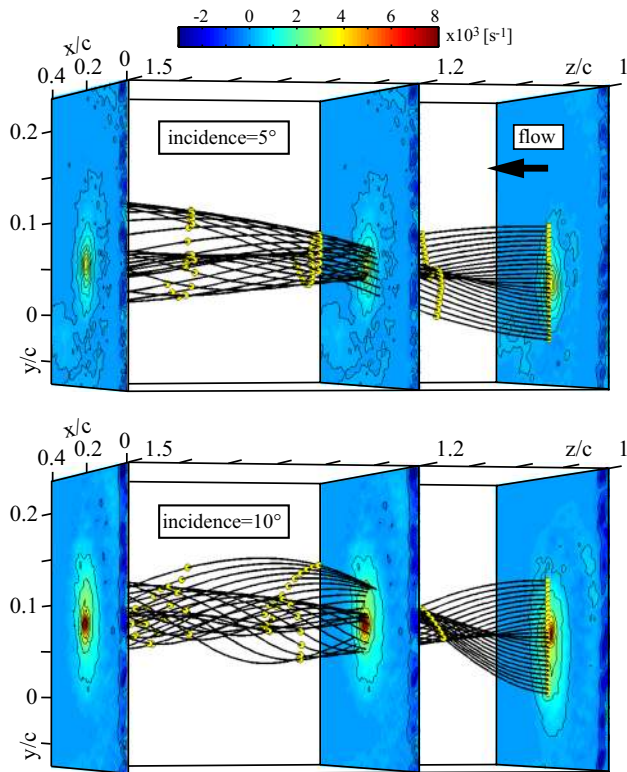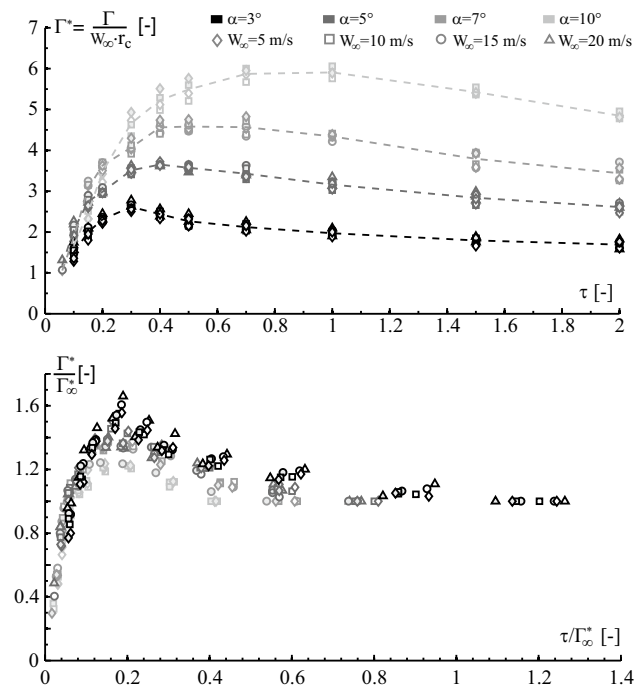
Fig. 10 3D streamlines with tracing particles in *yellow* showing the development of the TLV along the three measurement planes. The *colors* in the three measurement planes show the norm of the streamwise vorticity. Flow conditions: $W_\infty = 10$ m/s, $\tau = 1.5$, rough hydrofoil

Fig. 11 *Top* evolution of the normalized circulation, Γ^*, with the normalized clearance τ. The *dashed lines* are the mean values for each incidence angle. *Bottom* ratio of Γ^* over Γ^*_∞, the normalized circulation at $\tau = 2$, as a function of the normalized clearance divided by Γ^*_∞

is almost the same as the inlet velocity, and the particles stay in the same z plane as they coil around the vortex. In contrast, for the 10° incidence angle, the vortex core has a strong jet-like flow that deforms helically the originally aligned particles as they roll up into the vortex.

4.3 Circulation evolution

As the tip clearance is reduced, the characteristics of the TLV described in the previous section vary significantly. Figure 11 (top) summarizes the main effects of the confinement on the vortex circulation. The evolution is depicted for the combination of the four inlet velocities ($v = 5, 10, 15$ and 20 m/s) with four incidence angles ($\alpha = 3, 5, 7, 10°$) at two downstream positions ($z/c = 1$ and 1.2). For sake of readability, only the data of the rough hydrofoil are represented, but similar trends are obtained for the smooth hydrofoil. Following the derivation of the dimensionless pressure coefficient $C_{p_{min}}$ in Eq. (5), the circulation is normalized by r_c, the viscous core radius and W_∞, the inlet velocity. With this dimensionless circulation Γ^*, the results are independent of the inlet velocity and collapse into four groups according to their incidence angles. The figure
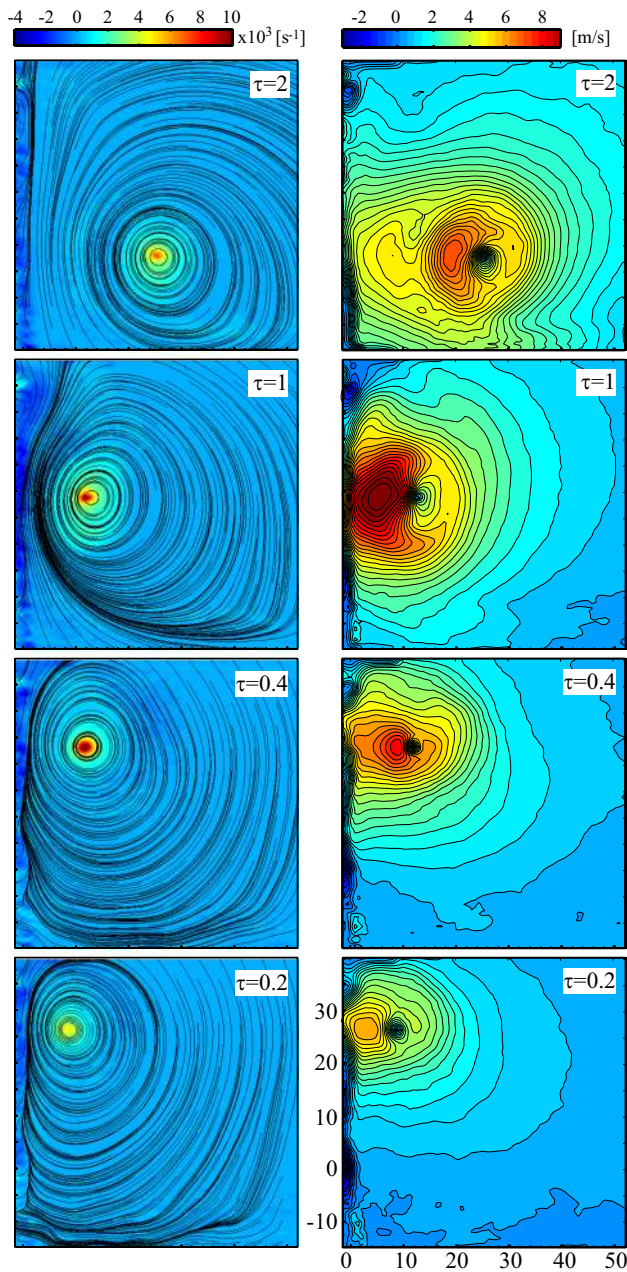
abscissa represents the normalized tip clearance, denoted by τ.

The existence of a specific gap width for which the vortex intensity reaches its maximum and is the most prone to generating cavitation is clearly revealed. Such cases should be typically avoided in hydraulic turbomachines. The value of this specific gap width depends on the incidence angle. For instance, the maximum vortex intensity is obtained for a specific τ value of about 0.3, 0.4, 0.5, 0.7 for incidence angles of 3°, 5°, 7° and 10°, respectively. Below those clearances, the vortex strength drops abruptly, whereas above them, it decreases slowly toward an asymptotic value for which influence of the wall becomes negligible. The limit gap width for which the influence of the wall vanishes depends on the foil incidence angle. Figure 11 (top) shows that this condition is probably not yet reached for the 10° incidence angle at $\tau = 2$, since the vortex intensity seems to further decrease at higher clearances. This indicates a stronger vortex–wall interaction at high incidences. Figure 11 (bottom) depicts the same data as Fig. 11 (top), but the dimensionless circulation Γ^* is normalized by the asymptotic value of the circulation at $\tau = 2$, denoted as Γ^*_∞. Similarly, the figure abscissa is taken as τ divided by Γ^*_∞. With this representation, all the results collapse together on a similar pattern. The confinement provokes a TLV peak

intensity 20–60 % higher than the value away from the wall when the dimensionless coefficient τ/Γ_∞^* equals ≈ 0.2. The evolution of the circulation correlates well with the flow visualizations in Fig. 5.

Figure 12 (left) details the vorticity map along with the 2D streamlines for the 10° incidence at four clearances. Each part of the figure represents an area of 50×50 mm surrounding the vortex. Outside the vortex core, the flow is i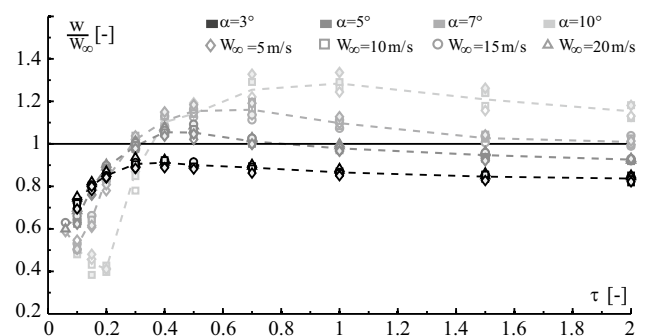rrotational except for the wall boundary-layer region. For the $\tau = 1$ case, the leakage vortex induces flow separation on the test section wall, as visible on the upper left of the figure. The wall boundary-layer with its counter-rotating vorticity is indeed entrained by the nearby TLV, as also reported by Miorini et al. (2012). As the gap is reduced, the TLV feels the neighboring wall and starts to migrate upward. The squeezing of the streamlines between the vortex center and the wall suggests a higher flow rate in this region. The inclination angle between the vortex axis and the measurement plane results in an apparent vortex asymmetry, as illustrated in Fig. 12 (right) with the isocontours of the circumferential velocity around the TLV axis. The contours depict a crescent-shaped region with a bump of high circumferential velocity between the wall and the TLV center, particularly visible in the $\tau = 1$ case where the inclination angle is ~10°. As a consequence, the location of the maximum vorticity does not correspond exactly to the vortex swirl center of rotation. On the contrary, the algorithm of Graftieaux for the identification of the vortex center (c.f. Sect. 3.2) is nearly unaffected by the inclination of the TLV with respect to the measurement plane.

4.4 Axial flow evolution in TLV

Figure 13 shows the ratio of the axial flow in the vortex center to the inlet velocity as a function of τ. Values smaller than one correspond to a wake-like profile, while values greater than one correspond to a jet-like behavior. The core axial flow evolution follows the vortex intensity evolution, with an increase in the first stage of the clearance reduction followed by an abrupt decline in the velocity magnitude in highly confined situations. For instance, the 7° incidence features a small axial velocity deficit at $\tau = 2$ which turns into a jet-like profile at $\tau = 0.7$ before resuming a wake-like profile at $\tau = 0.3$. As previously explained in the Sect. 4.2, the vortex core axial flow is the resulting balance between an inviscid flow effect that tends to accelerate
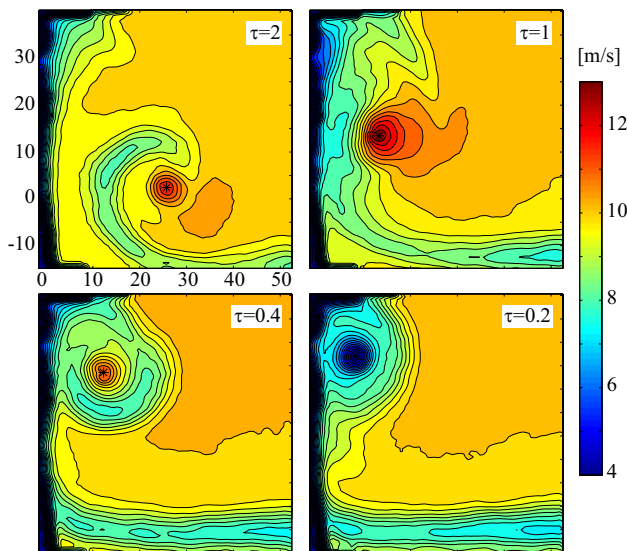

Fig. 12 *Left* 2D streamlines of the TLV for various gap widths with the norm of the streamwise vorticity. *Right* isocontours of circumferential velocity for various gap widths. Flow conditions: $W_\infty = 10$ m/s, incidence = 10°, $z/c = 1$, rough hydrofoil

Fig. 13 Evolution of the vortex core axial velocity, normalized by the inlet velocity, with the normalized clearance, τ. The *dashed lines* are the mean values for each incidence angle

the core flow, and the momentum deficit in the boundary-layer that rolls up into the vortex core, see Eq. (7). It is thus natural that the evolution of the axial velocity follows the change of vortex intensity with confinement. Figure 14 depicts the isocontours of the axial velocity for the 10° incidence and illustrates the velocity evolution as the gap is reduced. The test section wall boundary-layer is clearly visible on the left-hand side at $x = 0$ mm. With large clearance values, the TLV is surrounded by the foil wake that rolls up around the vortex axis. The velocity in the vortex center is a jet-like profile with a peak velocity 20 % higher than the inlet velocity. The vortex strength increases slightly as the clearance is reduced to $\tau = 1$ and the region in the TLV center with a velocity excess broadens while the foil wake is squeezed between the wall boundary-layer and the vortex center. At $\tau = 0.4$, the vortex starts to interact with the wall boundary-layer and a region of lower than the free-stream velocity completely surrounds the TLV. The vortex still keeps a small region of high axial velocity at its center. At $\tau = 0.2$, the vortex intensity becomes very low and the momentum defects in the boundary-layer overcome the core flow acceleration predicted by inviscid flow theory. As a consequence, a large wake-like region is present in the vortex core.

4.5 TLV position and wandering

Figure 15 (top) depicts the vortex center position with the corresponding gap width. x_c represents the spanwise distance between the lateral wall and the vortex center, while y_c is the distance in the upward direction between the
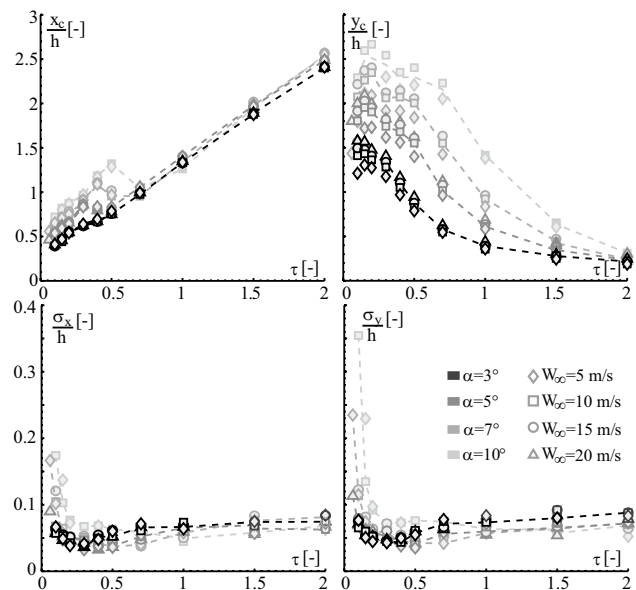
vortex center and the hydrofoil pitching axis, cf. Fig. 1. As the clearance is reduced, the vortex naturally moves closer to the test section wall. However, a sudden increase in x_c is observed around the clearance corresponding to the maximum vortex intensity—i.e., $\tau = 0.3, 0.4, 0.5, 0.7$ for the incidence angles of 3°, 5°, 7° and 10°—before the vortex center resumes its migration toward the wall. A clear physical explanation of this phenomenon is still lacking. It is assumed that the position of the vortices merging along the chord, as described in the Sect. 4.1, plays a key role in the TLV's final strength and position.

The wall proximity also affects the vortex vertical position, as depicted in Fig. 15. At large clearances, the vortex position is independent of the operating conditions (i.e., the incidence angle and inlet velocity). As the confinement increases, the vortex migrates upward. This displacement, which is more pronounced for high incidence angles, is characteristic of a vortex–wall interaction, modeled by an image vortex. The velocity induced by the image vortex depends both on the vortex strength and the proximity to the wall. Since the vortex strength diminishes at small clearances, this upward migration reaches a plateau, the value of which is linked to the foil incidence angle.

The wandering amplitude in the x- and y-directions relatively to the gap width is depicted in Fig. 15 (bottom) with the standard deviation of the mean vortex center location. The wandering amplitude remains fairly constant for all the clearance values, except in the most confined situations

Fig. 14 Isocontours of the axial velocity for different gap widths. Flow conditions: $W_\infty = 10$ m/s, incidence = 10°, $z/c = 1$, rough hydrofoil

Fig. 15 Evolution of the vortex center position (*top*) and wandering amplitude (*bottom*) with the normalized clearance τ. The *dashed lines* are the mean values for each incidence angle. The x-direction is represented on the *left-hand side,* while the y-direction is on the *right-hand side*

where it becomes very large (especially in the *y*-direction). No significant variation of the vortex core size was observed with the confinement.

5 Conclusion

Experiments are carried out on the influence of the clearance size on the TLV structure in a simplified case study. A NACA0009 hydrofoil is used as a generic blade in a water tunnel while the clearance between the blade tip and the wall is varied. The 3D velocity fields are measured using SPIV for different values of the upstream velocity, the incidence angle and a large number of tip clearances. The wandering of the vortex is filtered out in the averaging process of the velocity field to obtain accurate vortex properties. A total of 1,170 distinct flow configurations are tested, yielding an extensive experimental database.

High-speed flow visualizations, with cavitation used as a tracer, have shown qualitatively that both the vortex trajectory and intensity are strongly influenced by the wall proximity. It also highlighted the clearance flow alteration, turning into a wall jet as the tip clearance is reduced. SPIV measurements confirmed that the smaller the clearance, the more the vortex is pulled away from the hydrofoil. Moreover, it was observed that neither the vortex trajectory nor the wandering amplitude is altered by the TLV cavitation. Finally, the wake-like or jet-like nature of the axial flow profile in the vortex core is determined by the TLV intensity.

For each hydrofoil incidence angle, the systematic measurements clearly reveal the existence of a specific tip clearance for which the vortex intensity is maximum. By introducing a new dimensionless coefficient τ/Γ_∞^*, we show that the TLV circulation reaches a peak intensity for $\tau/\Gamma_\infty^* \approx 0.2$, which is 20–60 % higher than the unconfined case, regardless of the operating conditions. Such situations should be avoided in hydraulic axial turbomachinery, as they are the most prone to generating cavitation and lead to severe blade erosion.

References

Arndt RE (2002) Cavitation in vortical flows. Annu Rev Fluid Mech 34(1):143–175

Ausoni P, Zobeiri A, Avellan F, Farhat M (2012) The effects of a tripped turbulent boundary layer on vortex shedding from a blunt trailing edge hydrofoil. J Fluids Eng 134(5):051207–051207. doi:10.1115/1.4006700

Batchelor GK (1964) Axial flow in trailing line vortices. J Fluid Mech 20:645–658. doi:10.1017/S0022112064001446

Bhagwat MJ, Leishman JG (2002) Generalized viscous vortex model for application to free-vortex wake and aeroacoustic calculations. In: Annual forum proceedings-American Helicopter Society. American Helicopter Society, Inc, vol 58, pp 2042–2057

Bhagwat MJ, Ramasamy M (2012) Effect of tip vortex aperiodicity on measurement uncertainty. Exp Fluids 53(5):1191–1202

Bouillot P, Brina O, Ouared R, Lovblad K, Pereira VM, Farhat M (2014) Multi-time-lag PIV analysis of steady and pulsatile flows in a sidewall aneurysm. Exp Fluids 55(6):1–11

Boulon O, Callenaere M, Franc JP, Michel JM (1999) An experimental insight into the effect of confinement on tip vortex cavitation of an elliptical hydrofoil. J Fluid Mech 390:1–23

Chang NA, Yakushiji R, Dowling DR, Ceccio SL (2007) Cavitation visualization of vorticity bridging during the merger of co-rotating line vortices. Phys Fluids (1994-present) 19(5):058106. doi:10.1063/1.2732264

Chen G, Marble F, Greitzer E, Tan C (1991) Similarity analysis of compressor tip clearance flow structure. J Turbomach 113(2):260–269

Del Pino C, Parras L, Felli M, Fernandez-Feria R (2011) Structure of trailing vortices: comparison between particle image velocimetry measurements and theoretical models. Phys Fluids 23(013):602

Devenport WJ, Rife MC, Liapis SI, Follin GJ (1996) The structure and development of a wing-tip vortex. J Fluid Mech 312:67–106. doi:10.1017/S0022112096001929

Doligalski T, Smith C, Walker J (1994) Vortex interactions with walls. Annu Rev Fluid Mech 26(1):573–616

Fabre D, Fontane J, Brancher P, Le Dizes S, Roy C, Leweke T, Fernandez-Feria R, Parras L, del Pino C (2008) Synthesis on vortex meandering. Technical report, STREP project no. AST4-CT-2005-012238

Farrell K, Billet M (1994) A correlation of leakage vortex cavitation in axial-flow pumps. J Fluids Eng 116(3):551–557

Gopalan S, Katz J, Liu HL (2002) Effect of gap size on tip leakage cavitation inception, associated noise and flow structure. J Fluids Eng 124(4):994–1004

Graftieaux L, Michard M, Grosjean N (2001) Combining PIV, POD and vortex identification algorithms for the study of unsteady turbulent swirling flows. Meas Sci Technol 12:1422–1429. doi:10.1088/0957-0233/12/9/307

Green SI (1995) Fluid vortices: fluid mechanics and its applications, vol 30. Springer, Berlin

Iungo G, Skinner P, Buresti G (2009) Correction of wandering smoothing effects on static measurements of a wing-tip vortex. Exp Fluids 46(3):435–452. doi:10.1007/s00348-008-0569-2

Laborde R, Mory M, Chantrel P (1997) Tip clearance and tip vortex cavitation in an axial flow pump. J Fluids Eng 119(3):680–685

Le Guen A, Viot X, Billard JY, Fruman D (1997) Fluctuations des vitesses et biais spatial dans le tourbillon marginal. Sixièmes Journées de l'Hydrodynamique 317–328

Lee T, Pereira J (2010) Nature of wakelike and jetlike axial tip vortex flows. J Aircr 47(6):1946–1954

McCormick B (1962) On cavitation produced by a vortex trailing from a lifting surface. J Fluids Eng 84(3):369–378

Miorini RL, Wu H, Katz J (2012) The internal structure of the tip leakage vortex within the rotor of an axial waterjet pump. J Turbomach 134(3):031,018

Moore DW, Saffman PG (1973) Axial flow in laminar trailing vortices. Proc R Soc Lond Ser A Math Phys Sci 333(1595):491–508

Müller A, Dreyer M, Andreini N, Avellan F (2013) Draft tube discharge fluctuation during self-sustained pressure surge: fluorescent particle image velocimetry in two-phase flow. Exp Fluids 54(4):1–11. doi:10.1007/s00348-013-1514-6

Pasche S, Gallaire F, Dreyer M, Farhat M (2014) Obstacle-induced spiral vortex breakdown. Exp Fluids 55(8):1–11. doi:10.1007/s00348-014-1784-7

Prasad AK (2000) Stereoscopic particle image velocimetry. Exp Fluids 29(2):103–116. doi:10.1007/s003480000143

Roussopoulos K, Monkewitz PA (2000) Measurements of tip vortex characteristics and the effect of an anti-cavitation lip on a model Kaplan turbine blade. Flow Turbul Combust 64(2):119–144

Spalart PR (1998) Airplane trailing vortices. Annu Rev Fluid Mech 30(1):107–138

Vatistas GH, Kozel V, Mih W (1991) A simpler model for concentrated vortices. Exp Fluids 11(1):73–76

van der Wall BG, Richard H (2006) Analysis methodology for 3C-PIV data of rotary wing vortices. Exp Fluids 40:798–812. doi:10.1007/s00348-006-0117-x

Wang Y, Devenport WJ (2004) Wake of a compressor cascade with tip gap, part 2: effects of endwall motion. AIAA J 42(11):2332–2340

Westerweel J (2000) Theoretical analysis of the measurement precision in particle image velocimetry. Exp Fluids 29(1):S003–S012. doi:10.1007/s003480070002

Wu H, Tan D, Miorini RL, Katz J (2011) Three-dimensional flow structures and associated turbulence in the tip region of a water-jet pump rotor blade. Exp Fluids 51(6):1721–1737. doi:10.1007/s00348-011-1189-9